PHYSICAL REVIEW B **108**, 024408 (2023)

Observation of Griffiths phase, critical exponent analysis, and magnetic behavior in Bi-doped $La_{0.67}Ca_{0.33}MnO_3$

Arpit Gaur, Ankita Tiwari, Gurmeet Singh, and Rabindra Nath Mahato[*]
School of Physical Sciences, Jawaharlal Nehru University, New Delhi 110067, India

(Received 15 February 2023; revised 19 May 2023; accepted 22 June 2023; published 11 July 2023)

The nanocrystalline $La_{0.67-x}Bi_xCa_{0.33}MnO_3$ ($x = 0.0, 0.1$) samples were synthesized using a citrate complex method. The synthesized samples crystallizes in single phase and orthorhombic crystal structure with *Pbnm* space group. The nanocrystalline $La_{0.67}Ca_{0.33}MnO_3$ (LCMO) exhibits significant second-order paramagnetic (PM) to ferromagnetic (FM) phase transition, whereas weak second-order phase transition (SOPT) was observed for $La_{0.57}Bi_{0.1}Ca_{0.33}MnO_3$ (LBCMO). Magnetic entropy and Landau analysis have been used for the confirmation of order of transition in the vicinity of transition temperature (T_c). The Griffiths phase (GP), which was determined by the temperature-dependent inverse susceptibility (χ^{-1}) data, demonstrated a strong influence on La-site chemical substitution. Dimeron model is used to explain GP behavior for the samples. Temperature-dependent resistivity [$\rho(T)$] also suggests the existence of dimeron formation above metal-insulator transition temperature ($T > T_{MI}$). A an unusual magnetic state also have been observed within the nonlinear region of Arrott plots for $T > T_c$. Using information on the intrinsic magnetic field, the critical behavior of the LBCMO sample was examined close to its Curie temperature. The critical exponents β, γ, and δ are 0.3108, 1.02, and 4.2, respectively. The observed critical behavior is not following any universality class.

DOI: 10.1103/PhysRevB.108.024408

I. INTRODUCTION

Manganese perovskite oxides have been the subject of intensive study in recent years as a result of the various findings like large magnetoresistance (CMR), strong connection between the degrees of freedom for the lattice, charge, orbit, and spin, as well as other phenomena like metal-insulator transitions and Jahn-Teller (JT) distortions. Additionally, because of their chemical stability, reproducibility, and significant isothermal entropy change around ambient environment [1], they may find use in environmental-friendly and energy-efficient magnetic refrigeration [2–4]. It offers a perfect natural environment for research into the physics of strongly correlated magneto-electric systems in addition to potential applications. Therefore, a thorough investigation may result in a deeper comprehension of the underlying principles governing such systems as well as new opportunities for technology applications [5]. The standard chemical formula for the manganese perovskite oxides that are most frequently addressed is $A_{1-x}B_xMnO_3$, where A is rare earth trivalent cation (La, Nd, or Pr) and B is alkaline earth divalent cation (Ca, Sr, Ba, and Pb). A change in unit-cell volume occurs when a B divalent atom with a smaller or larger radius replaces the A site, process known as hole doping. To maintain charge equilibrium, the chemical substitution process causes part of the Mn^{3+} ions to be replaced by Mn^{4+} ions, called mixed-valence compound. As a result, the combination undergoes the double-exchange (DE) interaction (Mn^{3+}-O^{-2}-Mn^{4+}), leading to a metallic FM ground state, and super-exchange (SE) interactions [Mn^{3+}-O^{-2}-Mn^{3+}] and [Mn^{4+}-O^{-2}-Mn^{4+}], attributed to an insulating antiferromagnetic (AFM) ground state. Long-range Coulomb repulsion between T_2g electrons and JT distortion caused an insulating state, which is the underlying cause of AFM [6,7]. Additionally, the deformation of crystal structure, the ratio of Mn^{4+}/Mn^{3+}, the Mn-O bond length, Mn-O-Mn bond angle, and average cation size (A site) all significantly influence various physical properties of the complex.

As an intriguing phenomenon observed in both condensed matter physics and neuroscience, the Griffiths phase (GP) is also subject to the influence of these factors. In magnetism, GP development, which precedes the creation of ferromagnetic clusters (spatially distributed regions that are free of disorder and form ferromagnetically correlated spin arrangement in a finite region) well above ordering temperature T_c. It is frequently caused by quenched disorder and phase inhomogeneity. Quenched disorder in manganites can come from a variety of sources: (i) Size mismatch of A/B ions, this which results in variations in the Mn-O-Mn bond length and bond angle as well as local lattice distortion brought by Mn^{3+} ions (JT active). (ii) Chemical substitution in the A/B site caused changes in the Mn^{4+}/Mn^{3+} ratio and the tolerance factor [8]. Chemical substitution at the Mn location might also result in more disorder. In the context of Mott transitions, GP arises near the transition between a metal and an insulator due to the presence of disorder or inhomogeneities in the material. It characterized by local regions retaining some metallic character while the bulk material remains insulating [9,10]. Moreover, GP in neuroscience has been observed in the context of brain criticality, where the brain operates at a state that is balanced between order and chaos [11]. Now we wish

---

[*] Corresponding author: rnmahto@jnu.ac.in

to draw attention to the purpose of our effort before going forward. $LaMnO_3$ is insulating, multilayer antiferromagnet (AFM) compound in its ground state, in which the trivalent ions lanthanum and manganese, La^{3+} and Mn^{3+}, completely balance each other out. When divalent calcium was substituted into some of the lanthanum sites in the parent molecule, $LaMnO_3$, changing its magneto-electrical characteristics. This substitution leaves holes in the e_g state and changes some of the Mn^{3+} ions into Mn^{4+} ions. The remaining e_g electrons became mobile by moving between an adjacent Mn^{4+} and Mn^{3+} ion via the oxygen $2p$ orbital, creating an $O(2p)$-$Mn(e_g)$ band, which results in conducting behavior.

In this study, we present the impact of Bi^{3+} substitution on the structural, magnetic, and magneto-resistive properties of nanocrystalline $La_{0.67}Ca_{0.33}MnO_3$ at site A (La^{3+}). Given that Bi^{3+} and La^{3+} ions have almost comparable ionic radii and the same oxidation state, we do not anticipate any noticeable changes in their characteristics. Our experimental findings, however, clearly show a significant change in its characteristics. Therefore, it is presumed that the energy level arrangement and peculiar orbitals of Bi^{3+} are crucial in this scenario, and it has also been considered in various papers [12,13]. We present the impact of this assumption on the Griffiths singularity (also known as the Griffiths phase). Additionally, we have carried out a thorough examination of the critical exponents close to the PM to FM transition [14,15]. Critical exponents are crucial for understanding interaction processes close to the Curie temperature (T_c). According to earlier investigations on the critical behaviours around T_c, long-range mean-field theory was used to initially characterize the crucial behavior and to comprehend the interaction across a short-range manganites, 3D-Heisenberg model is widely utilized [16,17]. This article seeks to provide a thorough knowledge of LBCMO's critical behavior during the phase transition. The phase transition order was verified using entropy and Landau analysis before critical analysis. We have examined the critical behavior of the sample at T_c by making extremely precise magnetic measurements across a broad range of magnetic field and temperature using a variety of approaches, including the Kouvel-Fisher (KF) technique.

II. EXPERIMENTAL DETAILS

Manganese acetate tetrahydrate, pure bismuth nitrate, lanthanum nitrate, and calcium carbonate ($CaCO_3$) were used to create the nanocrystalline samples using the traditional sol-gel method. With the exception of calcium carbonate, each starting material was separately dissolved in deionized water. Nitric acid was used to dissolve calcium carbonate. Separately dissolved compounds were combined in a 1:3 ratio with citric acid. In order to get the final precursor, the mixture was heated until it reached the gel stage, then it was moved to a hot plate. The crystal structure along with phases of annealed samples were identified using x-ray diffraction (XRD) technology using a Rigaku Miniflex600 powder diffractometer. The Physical Properties Measurement System (PPMS Cryogenic Ltd.) has been used to conduct measurements of temperature and magnetic field dependence on magnetization. Magnetization data (M-H) for the first quadrant were gathered for LBCMO and LCMO in the temperature ranges of 196–280 K with varied temperature intervals and 210–275 K ($T = 5$ K), respectively. The materials' electrical resistivity was evaluated in an 8 T cryogenic free magnet (CFM) equipment using the traditional four-probe method.

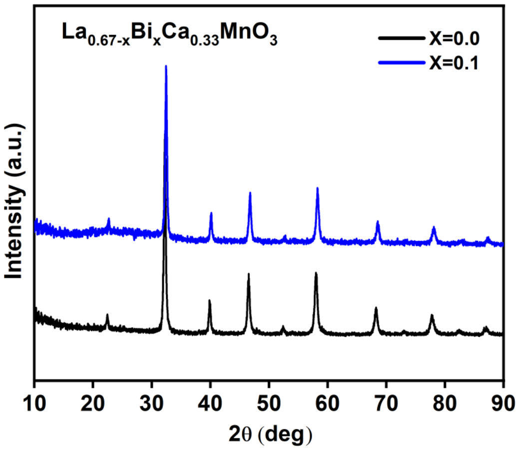

FIG. 1. XRD pattern of nanocrystalline at ambient temperature, LBCMO ($x = 0.0, 0.1$) samples.

III. RESULTS

A. Structural analysis

Using retveild refinement, the crystal structure along with phase analysis of the ambient-temperature XRD of LBCMO ($x = 0.0, 0.1$) have been examined. The observed XRD pattern show orthorhombic structure with *Pbnm* space group. Figure 1 displays the XRD patterns for both samples, which support the single phase nature of nanocrystalline materials. Lattice characteristics and convergence factors (χ^2) are listed in Table I. The data in Table I, with the exception of average bond length and average bond angle, were collected from Gaur *et al.* [18].

TABLE I. For the nanocrystalline LBCMO ($x = 0.0, 0.1$) samples: Information of the crystal structures along with fine-tuned lattice parameters, average bond length, average bond angle, cell volume, range (2θ), convergence factor (χ^2), as well as values for average crystallite size (D) has been listed.

Parameters	$x = 0.0$	$x = 0.1$
Crystal structure	orthorhombic	orthorhombic
Space group	*Pbnm*	*Pbnm*
a (Å)	5.4789	5.4291
b (Å)	5.4538	5.4416
c (Å)	7.7004	7.5767
$d_{\langle Mn-O\rangle}$ (Å)	1.9299	2.0096
⟨Mn-O-Mn⟩ (deg)	165.13	154.37
cell volume (Å^3)	230.097	223.841
2θ range (deg)	10–90	10–90
χ^2	1.68	2.19
D (nm)	25	29

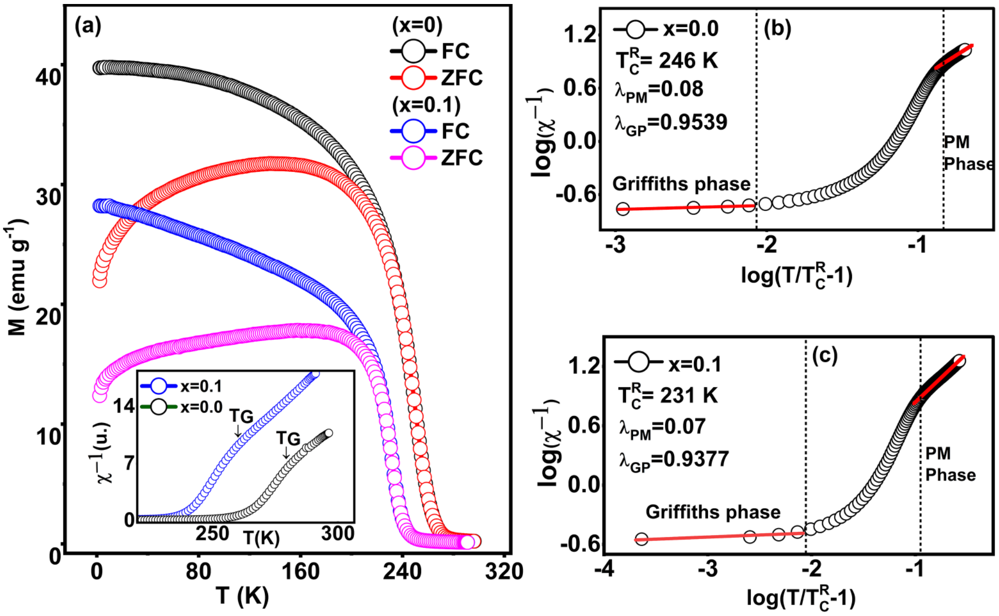

FIG. 2. For the LBCMO ($x = 0.0, 0.1$) samples, temperature-dependent field-cooled warming (FCW), and zero field-cooled warming (ZFCW) magnetization data are shown in (a), and the inset displays a inverse susceptibility (χ^{-1}) vs temperature (T) curve. The curves in (b) and (c) show $\log_{10}(\chi^{-1})$ vs $\log_{10}(T/\,T_c^R - 1)$; the red solid lines are linear fits to the experimental data for $x = 0.0$ and $x = 0.1$, respectively. Here λ_{GP}, exponent in GP; λ_{PM}, exponent in PM; T_c^R, the temperature at which random ferromagnet susceptibility departs from linear behavior; and T_G, Griffiths temperature.

B. Magnetic analysis

We have performed temperature-dependent magnetization (M-T) measurements of LBCMO ($x = 0.0, 0.1$) with an applied field of 50 mT in order to explore the phase transition between distinct magnetic phases {shown in Fig. 2(a), main panel of the figure has been taken from Gaur *et al.* [18]}, both samples have shown PM-FM phase transition. Our study of nanocrystalline LCMO found a transition temperature (T_c) of ~ 245 K, which is nearer to the reported $T_c \sim 250$ K [19]. However, for nanocrystalline LBCMO, we noticed a slightly reduced $T_c \sim 230$ K, as opposed to the $T_c \sim 244$ K reported for polycrystalline sample [13]. This is a common observation in nanocrystalline materials, as they typically exhibit lower transition temperatures than their polycrystalline counterparts [20]. Some of the magnetic parameters of distinct behavior listed in Table II. The transition temperature T_c got down by chemical substitution of La with Bi. We have compared the data for LBCMO to the parent compound LCMO in order to comprehend the observed behavior. With the chemical substitution of Bi^{3+} ions in the place of La^{3+} ions in the LCMO, neither the structural modification (length of the Mn-O bond and angle of the Mn-O-Mn bond) nor the charge balance Mn^{4+}/Mn^{3+} are anticipated to change because the ionic radius of the La and Bi ions ($r_{La} = 1.302$ Å and $r_{Bi} = 1.300$ Å) are very similar. This suggests that no change in DE interactions should be anticipated in the Bi-doped sample. However, the findings demonstrate that the magnetic and entropy characteristics of LCMO are significantly altered by the addition of Bi ions [18].

Bi–O bond is shorter than the La–O bond, despite the fact that the ionic radii of the Bi^{3+} and La^{3+} ions are equal. This can be explained by the fact that the Bi's 6*s* band, which has a significant dispersion, is thought to be important in covalent bonding [21]. Bi-O hybridization between the 6*s* of Bi and the 2*p* of O^{-2} orbitals is made more effective by the electronegativity of Bi. This Bi-O hybridization are evidenced by the lower bond angle (Mn-O-Mn) than that of the undoped sample, and modified Mn-O hybridization [12]. Little reduction in the bond angle (Mn-O-Mn) favors the AFM-SE interaction. Such structural distortion decreases the ferromagnetic double exchange interactions, the drop in Curie temperature reflects this fact.

Figure 3 shows the M-H isotherms for LBCMO sample close T_c with a field span of 0 to 5 T. Arrott plots (M^2 vs μ_0H/M plots) have also been used to study the order of phase transition depicted in Fig. 4; Fig. 4(a) has been taken from Gaur *et al.* [18]. According to Banerjee's criterion, a magnetic second order phase transition (SOPT) or magnetic first order phase transition (FOPT) is indicated by positive

TABLE II. Inverse susceptibility exponents (λ) along with characteristic temperatures, the range of GP follows, GP = $[(T_G\text{-}T_c)/T_c]*100$ for the LBCMO ($x = 0.0, 0.1$), magnetic characteristics including Curie-Weiss temperature [θ_P(K)] and effective magnetic moment [$\mu_{\text{eff}}(\mu_B/\text{fu})$] respectively.

Bi$_x$	$x = 0.0$	$x = 0.1$
T_c (K)	245	230
T_G(K)	273	249
T_c^R (K)	246	231
λ_{PM}	0.08	0.07
λ_{GP}	0.9539	0.9377
GP (%T_c)	11.4	8.2
θ_P (K)	260	233
$\mu_{\text{eff}}(\mu_B/\text{fu})$	8.96	8.7

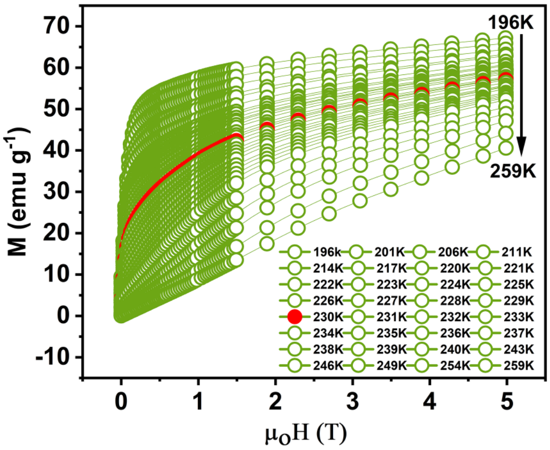

FIG. 3. Field dependent magnetization data (M-H) of LBCMO acquired at different temperatures between 196 K to 259 K, with an external- field span of 0–5 T.

and negative slopes on Arrott plots, respectively [22]. LCMO shows the magnetic SOPT as we can see positive slopes in the whole Arrott plot region in Fig. 4. Instance of LBCMO, the Arrott plot (Fig. 4) demonstrates that there is an region for $T \geqslant T_c$ at low fields (0–1.5 T) displaying negative slopes, but as field increases slopes turns positive. As slopes gradually shifts from negative to positive with increasing field strength, resulting in an "S" shaped curves. This behavior is indicative of a weak SOPT.We emphasize that weak SOPT does not necessarily imply any inherent weakness of the transition, but rather represents a specific behavior (S shape of Arrott plot at low magnetic field) for SOPT. We must first do more research into our claim using some of the other techniques we will be studying in Sec. III D before drawing any firm conclusions about the order of transition for LBCMO.

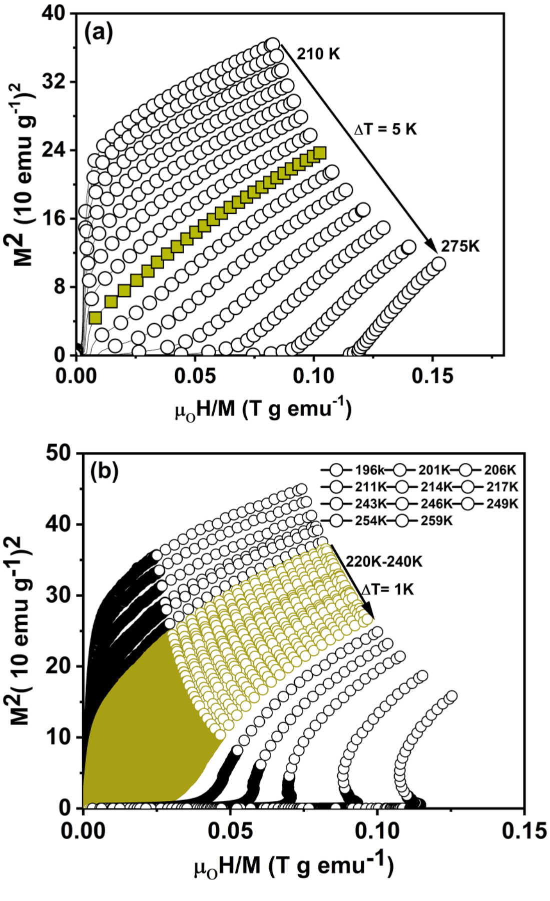

FIG. 4. [(a),(b)] M-H curves in the form of Arrott plots for LCMO and LBCMO over a range of temperatures.

1. Griffiths phase

The Griffiths phase (GP) is the transitional phase between the FM and PM phases, when inverse-susceptibility $[\chi^{-1}(T)]$ depicts a decline as a function of temperature [23]. Inset of Fig. 2(a) depicts the temperature dependence of $\chi^{-1}(T)$ derived from DC magnetization for LBCMO ($x = 0.0, 0.1$). The $\chi^{-1}(T)$ versus T curves for samples LBCMO ($x = 0.0, 0.1$), in the PM region, deviates from the linear Curie-Weiss (CW) behavior suggesting the presence of GP (finite-size clusters with FM coupled spins).

However, a static long-range order close to T_c would not emerge in the system as a whole. The exponent λ ($0 \leqslant \lambda \leqslant 1$) is usually used to define a Griffiths singularity, and the inverse susceptibility relationship with exponent λ is defined as

$$\chi^{-1} \propto \left(T - T_c^R\right)^{(1-\lambda)}. \tag{1}$$

T_c^R, the temperature at which random ferromagnet susceptibility departs from linear behavior. The GP-region may be measured using

$$\mathrm{GP} = \frac{T_G - T_c}{T_c} 100. \tag{2}$$

The Griffiths temperature (T_G), which is characterized as the start of a decline in $\chi^{-1}(T)$ for PM region. We have estimated the T_G, is by analyzing the maxima of the derivative of the inverse susceptibility with respect to temperature. According to theoretical findings, the power-law behavior represented by Eq. (1) is induced by the Griffiths-like phases. The preceding statement is in fact a modified version of the CW equation, and the λ denotes a departure from CW behavior as a result of the formation of FM clusters above T_c. The value of λ, on the other hand, is often zero in the pure PM zone. As the temperature descends from the higher temperature zone toward T_c, more clusters reach the FM ordering condition. According to Bray's generalized Griffiths concept of [24] bond distribution, In the temperature range T–T_c^R, the system enters the Griffiths phase when neither pure PM behavior nor long-range FM ordering are present. The PM region creates a number of tiny FM clusters of various sizes in a spatially dispersed region. χ^{-1} is represented as $\log_{10}\chi^{-1}$ vs $\log_{10}(T/T_c^R - 1)$ in order to explain our findings for comprehending the GP in the LBCMO ($x = 0.0, 0.1$) [shown in Figs. 2(b) and 2(c)]. The slopes of the linearly fitted data for the λ_{GP} (exponent in GP) and λ_{PM} (exponent in PM) regimes, respectively, have been used to calculate the values of GP and PM phase. The exact value of T_c^R determines the appropriate value of λ. Inaccurate T_c^R values will result in erroneous values for λ. We used the approach described elsewhere to determine the correct value of T_c^R [25]. In this technique, T_c^R is initially fixed at T_c, inverse susceptibility in the PM condition is fitted for λ_{PM}. The T_c^R value is then changed so that in the PM state, λ_{PM} is close to zero. GP converted into the conventional PM phase above the Griffiths temperature T_G, and χ^{-1} follows the CW equation. The value of T_c, T_G, T_c^R, λ_{PM}, λ_{GP}, and GP ($\%T_c$) tabulated in Table II. An extremely high value of GP represents the strong Griffiths singularity in the LBCMO ($x = 0.0, 0.1$) sample. We can clearly see that with Bi doping λ_{GP} is decreasing. It shows that Bi doping suppressing the formation of clustering, responsible for GP; GP ($\%T_c$) also suggesting the similar nature.

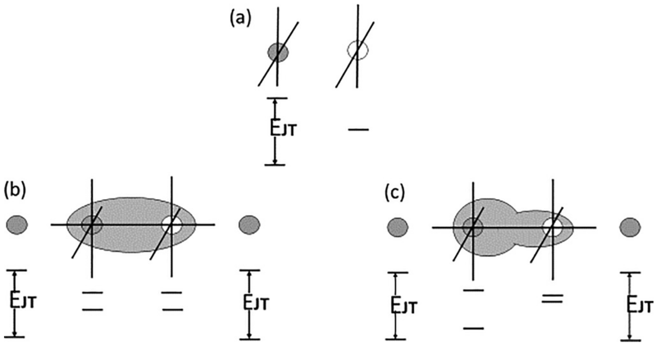

FIG. 5. Cartoon model for dimeron. (a) The Mn^{3+} site shown with grey circle and Mn^{4+} site shown with a white circle, and O atoms have not shown. E_{JT} is the splitting between energy levels of e_g electrons. In Case (b) One e_g electron shared by the paired Mn^{3+}-Mn^{4+} site is shown by the grey oval. when each of these site has Ca or La or both in the vicinity. Despite the fact that the Mn-O bond length (solid lines) on each of these sites are incomparable, the distortions on these two sites are equivalent, resulting in the same small JT splitting of the e_g levels. In (c) the grey distorted oval represent one electron shared between the paired Mn^{3+}-Mn^{4+} site when each of these site has Bi in the vicinity along with La or Ca or both. Each of these sites exhibits a minor but distinct JT splitting of the e_g levels and the Mn-O bond lengths (solid lines) and distortions on each of these sites are incomparable. In situations (b) and (c), two adjacent Mn^{3+} atoms on the left and right, each of which has one e_g electron, are having a larger distortion, leading to significant JT splittings of the e_g levels. A considerable barrier prevents an electron at the lowest e_g level on the left or right Mn sites from hopping onto the middle dimeron sites because of the significant difference in JT energies.

Now the question arises as to how Bi doping suppressing the formation of GP. Before reaching any conclusion we should emphasize that Bi doping does not change the the number of SE sites Mn^{3+}-O^{-2}-Mn^{3+} or Mn^{4+}-O^{-2}-Mn^{4+}, number of DE sites Mn^{3+}-O^{-2}-Mn^{4+}, and amount of JT active Mn^{3+} ions. Therefore, the short-range FM clustering that is important for GP formation should ideally not be impacted by Bi doping; however, this is not the case. The issue therefore becomes what phenomenon is behind the suppression of GP with Bi concentration? The possible reason behind the suppression of GP will be understood well once we know how such clusters are forming. Here we used a model called dimeron model where a pair of JT distorted (Mn^{3+}) and non-JT distorted (Mn^{4+}) sites produces a local distortion [26]. We designate this kind of distortion as a dimeron (paired Mn^{3+} and Mn^{4+}) and correlate such a distortion with two-site quasiparticle (polaron) [26,27]. Moreover, the temperature-dependent resistivity analysis also confirms the formation of dimeron (small polaron), which will be seen in Sec. III C. JT energies differ between a distorted JT active (one e_g electron with significant JT splitting) Mn^{3+} site and an undistorted JT nonactive (no e_g electron with no JT splitting) Mn^{4+} site. There is a very high barrier created by the disparity in JT energies between Mn^{3+} and Mn^{4+}, pictorial depiction can be seen in Fig. 5(a). An e_g electron from occupied JT distorted Mn^{3+} site 1 moves to a vacant and undistorted Mn^{4+} site 2, In the meantime unoccupied site 2 starts to distort and occupied site 1 starts to undistort. We call such state an intermediate local distorted state (ILDS) as this state has a local distortion in between the distorted JT active and undistorted JT nonactive site. When the two sites 1 and 2 relax, they approach their new equilibrium local state (NELS). Now there will be two possibilities of NELS: (i) First NELS state (comparable JT splitting or no JT barrier): there would be virtually no energy barrier between the two paired Mn sites, the JT splitting of the two sites would be roughly equal, and electron hopping between them would be extremely quick. On each site, there will be a little quasi-equilibrium distortion. Figure 5(b) is a cartoon explaining the above mentioned phenomenon. When compared to the JT active Mn^{3+} site, these locally paired distorted Mn sites would behave more like quasiparticles and share one e_g electron almost equally between the two Mn sites. This smallest unit permits both quick back-and-forth hopping of e_g electron, which will lead to strong double exchange FM coupling and high mobility of dimeron. First NELS state will be referred as a strong dimeron state because of the strong DE coupling and high mobility. (ii) Second NELS state (incomparable JT splitting or finite JT barrier): there would be a finite JT barrier between the two paired Mn sites, the JT splitting of these two sites would not be same. This local quasiparticle, which has one e_g electron shared across two Mn sites unequally and electron hopping between them would not be quick that will lead to a weak double exchange FM coupling and low mobility of dimeron. A cartoon explaining the above mentioned phenomenon is shown in Fig. 5(c). Second NELS state will be referred to as a weak dimeron state because of the low mobility and low DE coupling. Strong dimeron state (high mobility) is forming when there are La or Ca or both elements surrounding the dimeron. Weak dimeron (low mobility) state is forming when there are one Bi or more than one Bi atom surrounding the dimeron. The establishment of a second NELS state with a weak DE interaction weakens the nucleation of a short-range FM clustering, which results in the suppression of GP. The first NELS state's strong DE interaction favours the nucleation of short-range FM clustering, which leads to GP. A strong GP is emerging in the LCMO scenario due to the creation of the first NELS state, whereas in the case of Bi-doped LBCMO, the GP state is being diluted or suppressed due to the formation of the second NELS state. Now, the issue is: What role is Bi playing in weakening the clustering that is causing GP to be suppressed? Bi's high electronegativity makes the hybridization of the 6s orbital of Bi^{3+} and the 2p orbital of O^{-2} more effective than that of Mn-O. This hybridization is evidenced by the smaller bond angle of Mn-O-Mn, which favors the localization of the e_g electron and weakens the DE interaction, which in turn

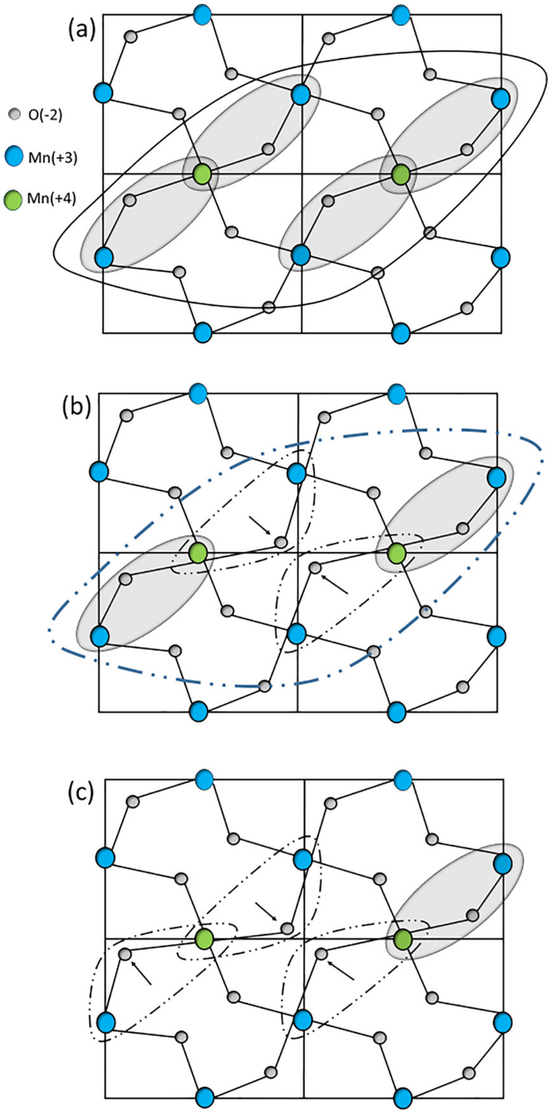

FIG. 6. [(a)–(c)] Griffiths phase formation and clustering phenomenon.

weakens the clustering and suppresses GP. The whole process can be understood well by a model given by Downward *et al.* [Fig. 6(a)–6(c)] [26]. In Fig. 6(a), orthorhombic (given that the examined compounds' main phase) unit cell has been considered for the LBCMO ($x = 0.0, 0.1$) samples, where the Mn atoms shown along withoxygen in the ab plane. The JT distorted (non-JT distorted) lattice locations are described by the Mn^{3+}(Mn^{4+} ions. Figure 6(a) shows the pair of Mn^{3+} and Mn^{4+}, assuming Ca or La or Both in the vicinity, making a dimeron encircled with grey oval and ferromagnetic clusters are created by the agglomerated dimerons (shown with black curve). Figure 6(b) indicate that, if dimeron has Bi atom in the vicinity, that weaken the dimeron as shown by black dashed curves, thus DE above $T > T_c$ and clustering also getting affected. Weakening of clustering also has been shown by dashed blue curve. Figure 6(c) shows that ferromagnetic clustering started diminishing in size, and as a result the GP-region will be diminished.

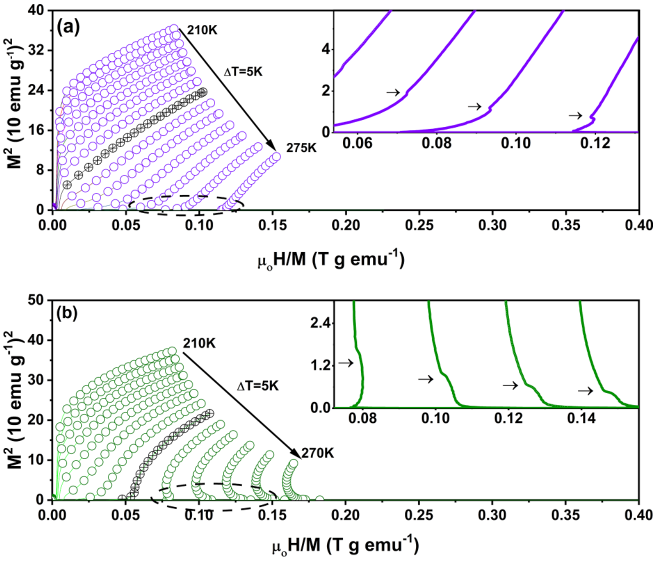

FIG. 7. [(a),(b)] Arrott plots for LCMO and LBCMO respectively and the inset figures have shown enlarged view of Arrott plot with in the dashed oval shape.

2. *An unusual new magnetic state in paramagnetic region*

According Chauhan *et al.* [28], we may analyze different magnetic states in the nonlinear part (regions with low field and low temperature) of the M-H curve using the Arrott plot. Here we have shown Arrott plots for LCMO and LBCMO samples in Fig. 7 and enlarged part in the inset shows the region of Arrott plot at low field for $T > T_c$. Here one can observe a kind of kink behavior [shown by arrows in insets of Fig. 7(a) and 7(b)] at every temperature for $T > T_c$ (paramagnetic region). This kink region, reflected in Arrott plot, seems like a boundary between nonlinear and linear part of the curve (transition between nonlinear to liner M-H region). It seems that nonlinear part exist because of the two possibilities: first is related to Griffiths phase formation or clustering of short range FM interaction and second possibility suggest a field induced phenomenon. The linear part corresponds to pure paramagnetic state for $T > T_c$.

C. Electrical transport studies

Both the LBCMO ($x = 0.0, 0.1$) samples show metal-insulator transition (T_{MI}) at 245 K and 230 K respectively in the absence of external magnetic field and it can be seen in Fig. 8(a) (taken from Gaur *et al.* [18]). Magnetic ordering temperature and metal-insulator transition temperature (T_{MI}) are almost same, which can be attributed to strong magnetotransport coupling. Bi-doped sample LBCMO shows very high resistivity compared to undoped sample LCMO, which basically mean that conduction mechanism in case of LBCMO greatly affected by Bi^{3+} doping. The reason could be 6*s* lone pair of electrons in Bi^{3+}, it affects the hybridization of Bi with O in comparison to Ca/La in such a way that it promotes localized state of e_g electron and some grain boundary effect will also add to it. For $T > T_{MI}$ we have used VRH and SPH model to explain the conduction mechanism and it turned out that SPH model fitted well in the temperature range

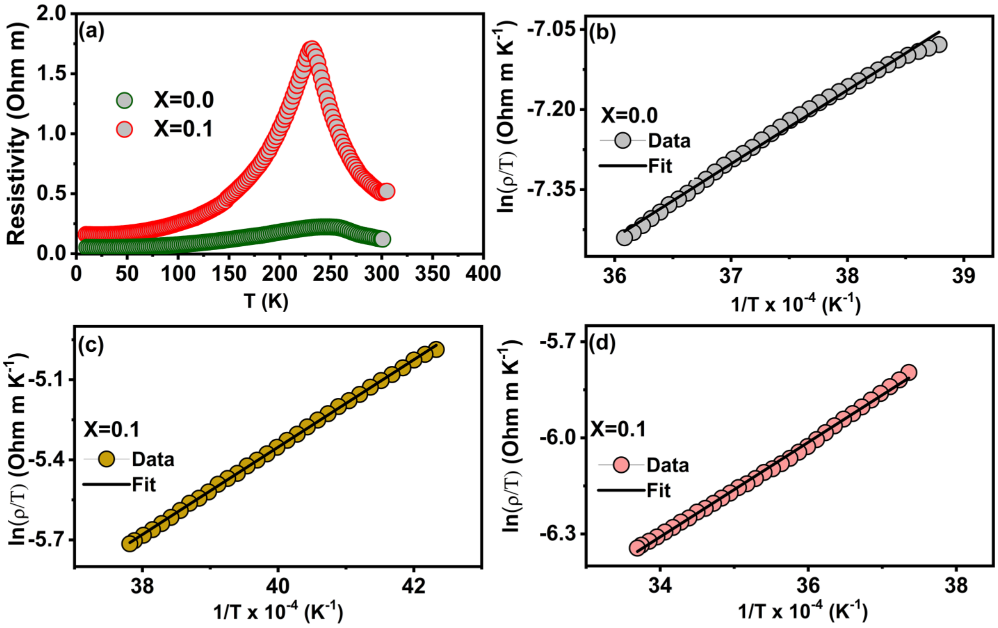

FIG. 8. (a) Temperature dependent resistivity for LBCMO ($x = 0.0, 0.1$) without magnetic field. (b) SPH fit for LCMO in temperature range 250 K–275 K. (c) and (d) shows the SPH fit for LBCMO within the temperature range 235 K–260 K and 265 K–290 K respectively.

235–290 K. The temperature range (T_R) for fitting the resistivity part has been chosen considering the GP, $T_R \sim (T_G - T_{MI})$. SPH model equation can be written as

$$\rho = AT \exp \frac{E_a}{k_B T}, \tag{3}$$

where ρ, A, E_a, and T represents the resistivity, coefficients of resistivity, activation energy and characteristic temperature respectively. Fitted temperature range, coefficient of resistivity (A) and activation energy values, for both the samples, have been listed in the Table III. In essence, the fitted data reveals that the conduction process is being carried out by a small polaron (dimeron) above $T > T_{MI}$. This confirms our assertion that dimeron production occurs after transition. Two conclusions may be drawn from the temperature-dependent resistivity fitted data above T_{MI}. (i) Since LCMO has a lower activation energy than LBCMO, its conduction mechanism is largely driven by a dimeron in a high mobility state; Fig. 5(b) represent the high mobility state of dimeron (e_g electron of dimeron is delocalized for paired Mn site) whereas in LBCMO it is happening by low mobility state of dimeron, Fig. 5(c) represents the low mobility state of dimeron (e_g electron of dimeron is localized more towards Mn^{3+} than Mn^{4+} site). (ii) High activation energy has been observed in temperature range $T_R \sim (T_G - T_{MI})$ than $T > T_G$. It means that at high temperature, thermal energy helping the e_g electron to cross the JT barrier, which lead to a more mobile dimeron state.

D. Does LBCMO show SOPT?

As we can see the Arrott plot for LBCMO in Fig. 4 (range 196–259 K) suggesting that it looks like a first-order phase transition considering Banerjee criteria because we are getting a region of negative slopes at high temperature and low field. For critical analysis, we will be focusing in the vicinity of T_c from 220 K to 240 K. Hence, before detailed critical analysis, in the vicinity of transition-temperature (T_c), ordering of magnetic phase transition must be clearly established. Here, we employ two separate techniques, entropy analysis [29–32] and Landau analysis [33], to ascertain the LBCMO's order of phase transition.

1. *Entropy analysis*

(i) The magnetic entropy change $|\Delta S_M|$ of the LBCMO around the T_c may be calculated with the help of Maxwell's thermodynamic relation and is given by [28]

$$\Delta S_M(\mu_0 H, T) = \int_0^{\mu_0 H} \left(\frac{\partial M(\mu_0 H, T)}{\partial T} \right)_H d(\mu_0 H), \tag{4}$$

where H is the external magnetic field, M magnetization, and μ_0 the permeability of vacuum. Due to effective spin ordering, manganites have a significant magnetic entropy shift

TABLE III. Fitted parameters for the LBCMO ($x = 0.0, 0.1$) samples were obtained for the SPH model.

x		$A \times 10^{-6}$ (Ω m)	e_a/k_B (K)	e_a (mev)	Figure
0.0	T_R(K) = 250–275 K	4.0771	1380.66	119.08	8(b)
0.1	T_R(K) = 235–260 K	6.7677	1637.71	141.25	8(c)
	$T > T_R$(K) = 265–290 K	11.981	1477.27	127.41	8(d)

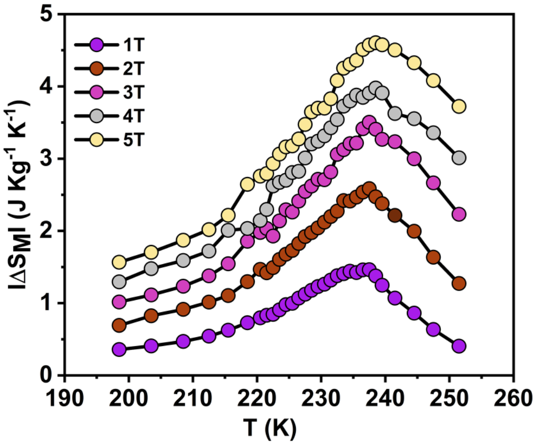

FIG. 9. For the nanocrystalline LBCMO sample, the variation in magnetic entropy ($|\Delta S_M|$) with temperature at varied applied fields.

near T_c [34–36]. A spin-lattice coupling contribution is mostly responsible for the significant change in entropy $|\Delta S_M|$ of perovskite material. The magnitude of the $|\Delta S_M|$ increases steadily as the applied magnetic field is increased. Nonmonotonic behavior of entropy change $|\Delta S_M|$ with temperature is also an indication of the SOPT; Fig. 9 shows the same. We further exploited the rescaling of $|\Delta S_M|$ to guarantee the LBCMO's phase transition ordering. In case of SOPT, rescaled $|\Delta S_M|$ curves must collapse into single universal curve [29,30,32]. Franco *et al.* have theoretically shown that such a universal curve exists for a SOPT [29]. A SOPT's immediate neighbourhood can scale a number of physical characteristics [37]. It has been discussed how to scale $|\Delta S_M|$ phenomenologically. To do this in a phenomenological manner, all the $|\Delta S_M|$ would be normalized by the greatest value of the $|\Delta S_M|$, i.e., $\Delta|S_M^{\text{peak}}|$, which occurs at T_c. Reference temperature should be chosen such that $|\Delta S_M(T_r)|/|\Delta S_M^{\text{peak}}| \geqslant K$ in order to rescale the temperature axis. K must fall between the range of $0 < K \leqslant 1$ [38], where K is the ratio of entropy changes at two different reference temperature. Two reference temperatures $T_{r_1} < T_c$ and $T_{r_2} > T_c$ have been selected so that $|\Delta S_M(T_{r_1})|/|\Delta S_M^{\text{peak}}| = |\Delta S_M(T_{r_2})|/|\Delta S_M^{\text{peak}}| = 0.7$ and, respectively. The definition of rescaled temperature, say θ, axis is

$$\begin{aligned} \theta &= -(T - T_c)/(T_{r_1} - T_c), \quad T \leqslant T_c \\ &= (T - T_c)/(T_{r_2} - T_c), \quad T > T_c. \end{aligned} \tag{5}$$

Figure 10 displays the entropy curve that has been scaled within the field span 1–5 T. The presence of the LBCMO's SOPT is supported by the finding that each entropy curve collapses onto a single universal curve.

(ii) In the literature, a different approach to determining the magnetic order of phase transition was published [39,40]. In this method, the field dependency of the sample's $|\Delta S_M|$ was established by using the relation $|\Delta S_M| = a(\mu_0 H)^n$, where "$n$" is a magnetic order-related exponent and "a" is a constant. The exponent (n) for single-phase ferromagnets depend on magnetic-field and temperature [41,42] and represented by the following notation:

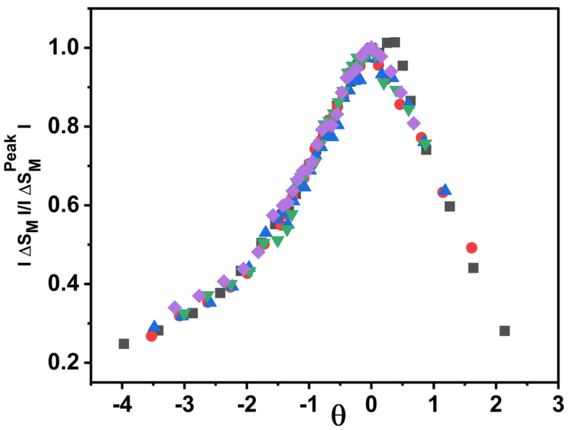

FIG. 10. The rescaled entropy curves in the field range for the nanocrystalline LBCMO sample.

$$n(T, H) = \frac{d \ln |\Delta S_M(T, H)|}{d \ln H}. \tag{6}$$

The values of $n(T, H)$ describe the magnetic order of ferromagnets. The sample is in a multidomain condition for extremely tiny fields, hence such exponent values should not be taken into account. In-depth research has been done on the temperature dependence of n for SOPT materials [43,44]. In the case of SOPT, value of n for $T < T_c$ and $T > T_c$ tends to 1 and 2, respectively. The presence of the overshoot of n over 2 is the condition to identify that the transition is a FOPT. Here, in Fig. 11, we see that n(max) is less than 2, which is in line with our prior claims of a SOPT. According to mean-field theory, for ferromagnets with long-range magnetic order, $n(T, H)$ at T_c is independent of H and reaches the value with $n(T) = 2/3$ [45]. However, in every other scenario, the minimum value is different and linked to the material's critical exponents $n = 1 + \frac{1}{\delta}(1 - \frac{1}{\beta})$, assuming that the applied field is sufficient to maintain the material within the critical region [46]. From Fig. 11, n(min) is valued to be minimal between

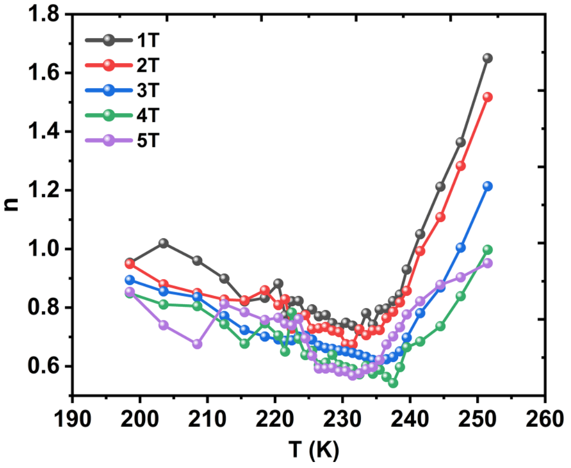

FIG. 11. For various magnetic fields, the temperature variation of exponent $n(T, H)$ for LBCMO sample.

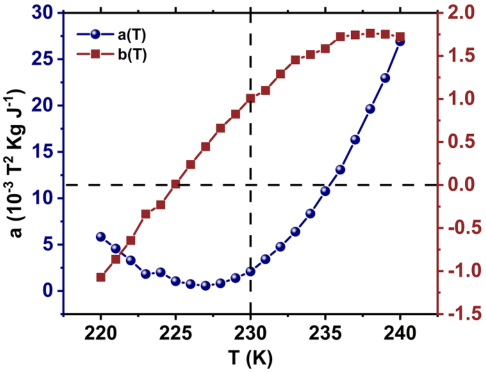

FIG. 12. The nanocrystalline LBCMO sample's Landau coefficients [a(T) and b(T)] temperature dependency.

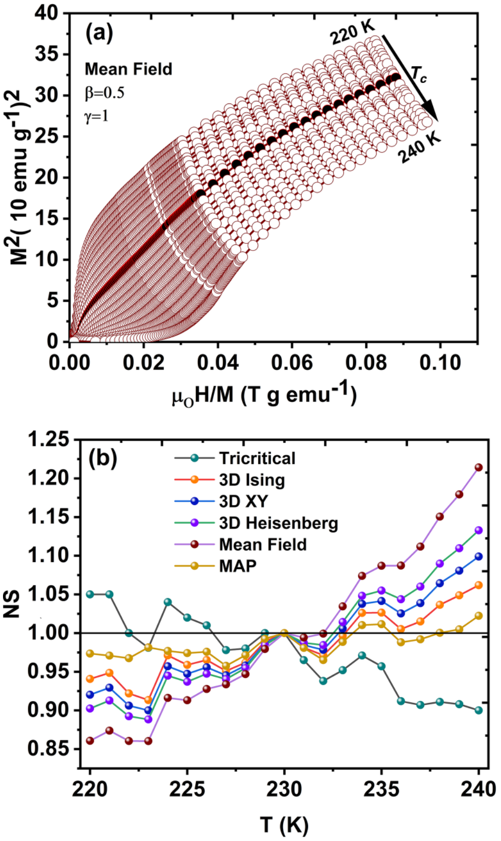

FIG. 13. (a) The M-H curves for the nanocrystalline LBCMO sample at various temperatures between 220 K and 240 K are shown in form of Arrott plot (M^2 vs $\mu_0 H/\mathrm{M}$). (b) Normalized slopes [NS = S(T)/$S(T_c)$] as a function of temperature for several models, $S(T) = dM^{1/\beta}/d(\mu_0 H/M)^{1/\gamma}$, $S(T_c)$ is the slope at T_c.

0.6 and 0.7 for various applied fields instead a constant. It tells us that LBCMO does not follow mean-field approach.

2. *Landau analysis*

A power series in terms of the order parameter M may be used to determine the magnetic free energy *F(M,T)* of a ferromagnet [47],

$$F(M, T) = F(0) + \frac{a(T)}{2}M^2 + \frac{b(T)}{4}M^4 + \frac{c(T)}{6}M^6 + \cdots - \mu_0 HM, \tag{7}$$

where $a(T)$, $b(T)$, and $c(T)$ are Landau coefficients. We can determine the kind of the phase transition near T_c using $F(M, T)$. The thermodynamic potential is minimized to create the equilibrium state, $\partial \mathrm{F}(M, T)/\partial \mathrm{M} = 0$ and resulting in

$$\mu_0 H = a(T)M + b(T)M^3 + c(T)M^5. \tag{8}$$

Temperature-dependent Landau coefficients $a(T)$ and $b(T)$ allowed us to differentiate between FOPT and SOPT using Eq. (8). The FOPT corresponds to the negative value of $b(T)$ at T_c, while the SOPT corresponds to the positive value. T_c of the sample should be associated with the minima of $a(T)$. Equation (7) was used to fit the magnetic isotherms to derive the Landau coefficient $a(T)$ and $b(T)$. Figure 12 display how Landau coefficients change with temperature. $b(T)$ is having a positive value at T_c as well as passing from zero line at temperature T_0 and T_c of LBCMO is associated with minima of $a(T)$. This suggest us that LBCMO shows SOPT close to T_c.

E. Critical analysis and scaling

Understanding the mechanics behind various magnetic phases is made possible by a certain universality class. Mean-field model (MF), tricritical mean-field model (TMF), three-dimensional Heisenberg model (3D-H), three-dimensional Ising model (3D-I), and three-dimensional XY model (3D-XY) are five universality classes, which are used to characterize the phase transition in magnetic materials. In general, the critical exponents and the T_c for the long-range mean-field approximation may be calculated using the Arrott plot (M^2 vs μ_0H/M) but one must move beyond the MF approximation if the M-H data at various temperatures provided as M^2 vs μ_0H/M (Arrott plot) are not parallel. As a result, long-range universality classes (UCs) like long-range tricritical mean field and long-range mean field can be disregarded.

Figure 13(a) displays the LBCMO Arrott plot near T_c. Since the Arrott plot exhibits nonlinear behavior even in the higher field area then long-range interactions (MF model $\beta = 0.5$ and $\gamma = 1$) are probably invalid in LBCMO. The SOPT is represented by the positive value of slope in the Arrott plot, whereas the FOPT is represented by the negative value of slope. As a result, the Arrott plot again matches the results of the Landau and entropy analyses and so supports the SOPT. The modified Arrott plots (MAPs) have been the main emphasis in order to determine the right critical exponents (β and γ). α, β, γ, and δ are variables (critical exponents) to study the critical behavior of such system, which is showing SOPT and these same variables distinguish between different UCs. The fact that all UCs include fairly comparable δ value means that it is difficult to compare many models with single variable δ (see Table IV).

The 3D-I, 3D-XY, TMF, and 3D-H model's respective value for δ are 4.82, 4.81, 4, and 4.8 [48–50]. The initial susceptibility $\chi_0(T)$ and the spontaneous magnetization $M_S(T)$ exhibit universal scaling laws as a result of the advent of divergence of the correlation length $\xi = \xi_0|T - T_c/T_c|^{-\nu}$ in the vicinity of the T_c. The mathematical definitions of critical exponents around T_c from magnetization are defined as

TABLE IV. Comparison of the nanocrystalline LBCMO sample's critical exponents β, γ, and δ with several theoretical models. MAPs, Modified Arrott plots; KF, Kouvel-Fisher; CI, critical isotherm; and EA, entropy analysis.

	Method	T_c (K)	α	β	γ	δ
(Theory)						
Tricritical mean field [49]			0	0.25	1	5
3D Ising ($d = 3$, $n = 1$) [48,49]			0.11	0.325	1.241	4.82
3D XY ($d = 3$, $n = 2$) [48,49]			–0.007	0.346	1.316	4.81
3D Heisenberg ($d = 3$, $n = 3$) [48,49]			–0.115	0.365	1.386	4.8
(Experiment)						
LBCMO	MAPs	230 ± 0.2		0.3108 ± 0.001		
		230 ± 0.06			1.02 ± 0.003	
	CI					4.2
	KF	229.84 ± 0.1		0.30954 ± 0.0003		
		230 ± 0.002			1.016 ± 0.001	
	EA			0.344	1.11	

follows in accordance with the universal scaling hypothesis [51,52]:

$$M_S(T) = M_0(-\epsilon)^{\beta}, \quad \epsilon < 0,\ T < T_c, \tag{9}$$

$$\chi_0^{-1} = (h_0/M_0)(\epsilon)^{\gamma}, \quad \epsilon > 0,\ T > T_c, \tag{10}$$

$$M = DH^{1/\delta}, \quad \epsilon = 0,\ T = T_c, \tag{11}$$

And taking the derivative of Eq. (9),

$$\frac{dM_S(T)}{dT} = -\beta M_0(|\epsilon|)^{\beta-1}, \tag{12}$$

where $\epsilon = \frac{T-T_c}{T_c}$ is the reduced temperature and : M_0, M_0/h_0, and D are critical amplitudes. The Arrott-Noakes equation of state [54] in the asymptotic region $|\epsilon| < 0.1$ is

$$(H/M)^{1/\gamma} = (T - T_c)/T_c + (M/M_1)^{1/\beta}, \tag{13}$$

where β and γ are critical exponents and the material constant M_1 is used. The equation of magnetic state can be written as [49]

$$M(H, \epsilon) = \epsilon^{\beta} f_{\pm}(H/\epsilon^{(\beta+\gamma)}), \tag{14}$$

where $T > T_c$ defines f_+ and $T < T_c$ defines f_-. Rushbrooke and Widom's scaling relationship may be used to provide the relationship between critical exponents [51,55],

$$\alpha + 2\beta + \gamma = 2, \tag{15}$$

$$\delta = 1 + \frac{\gamma}{\beta}. \tag{16}$$

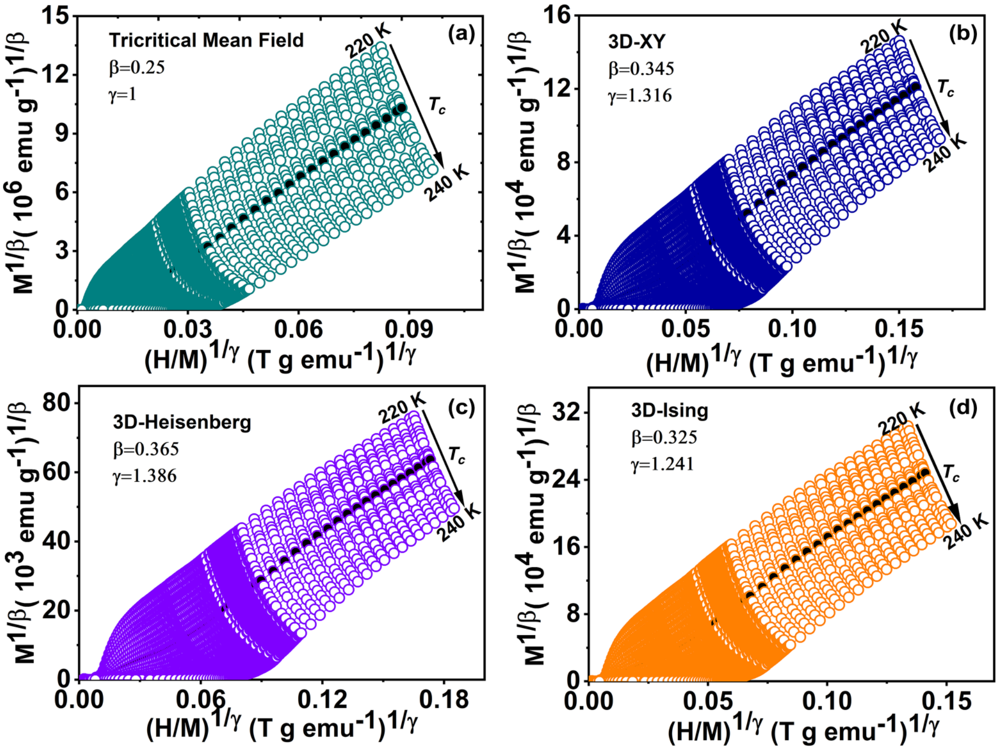

FIG. 14. The isotherms $of (M)^{1/\beta}$ vs $(\mu_0 H/M)^{1/\gamma}$ with (a) TMF, (b) 3D-XY (c) 3D-H, and (d) 3D-I.

Thus, by fitting $M_S(T)$ and $\chi_0^{-1}(T)$ using Eqs. (9) and (10), and MAPs $[(M)^{1/\beta}$ vs $(\mu_0 H/M)^{1/\gamma}]$, critical exponents β and γ may be derived. Using Eq. (11), M-H curve plotted at T_c will help us to calculate critical exponent δ separately.

To build the MAPs, we selected four distinct types of three-dimensional (3D) crucial exponents (β, γ) [49], which correspond to the 3D-H (0.365, 1.386), the 3D-I (0.325, 1.24), the 3D-XY (0.346, 1.316), and TMF (0.25, 1). All of the models display quasistraight lines for LBCMO (Fig. 14). Selecting the best model to evaluate the crucial exponents is challenging in this circumstance. We have employed the normalized slope (NS) technique to select the most suited model that captures the system. We have estimated their normalized slopes (NS) using this technique, where the slope $S(T) = dM^{1/\beta}/d(\mu_0 H/M)^{1/\gamma}$ [Fig. 13(b)]. NS [NS $= S(T)/S(T_c)$] should always be 1 if the MAPs display a succession of parallel lines with the same slope [53]. The best model, which has a closest fit to 1 over the chosen temperature range is clearly the 3D-I, as shown in Fig. 13(b). Critical exponent of 3D-I will be used as starting exponents for $M_S(T, 0)$ and $\chi_0^{-1}(T, 0)$ to get exact critical exponents.

The correct values $M_S(T, 0)$ and $\chi_0^{-1}(T, 0)$ in the MAPs of LBCMO generated for the 3D Ising model are provided by the intercepts with the axes $M^{1/\beta}$ and $(H/M)^{1/\gamma}$ gained by the linear extrapolation from the high field region [Fig. 14(d)]. Fitting these values of $M_S(T, 0)$ and $\chi_0^{-1}(T, 0)$ to Eqs. (9) and (10) results in one set of β and γ. To obtain the exact exponents (β and γ), an iterative method has been used [54]. The critical exponents for LBCMO using this technique are as follows: According to Fig. 15(a), $\beta = 0.3108 \pm 0.001$ with $T_c = 230 \pm 0.2$ K and $\gamma = 1.02 \pm 0.003$ with T_c=230 ± 0.06 K. Again, the Kouvel-Fisher (KF) technique [56] may be utilized to determine the critical exponents and with more accuracy, as stated by

$$\frac{M_S(T)}{dM_S(T)/dT} = \frac{T - T_c}{\beta}, \tag{17}$$

$$\frac{\chi_0^{-1}(T)}{d\chi_0^{-1}(T)/d(T)} = \frac{T - T_c}{\gamma}. \tag{18}$$

The $M_S(dM_S(T)/dT)^{-1}$ vs T along with $\chi_0^{-1}(d\chi_0^{-1}/d(T))^{-1}$ vs T will results in a straight line with slopes of $1/\beta$ and $1/\gamma$, respectively, and the intercepts on the temperature axis will provide the value T_c, per the KF method. According to the linear fitting of the $M_S(dM_S(T)/dT)^{-1}$ and $\chi_0^{-1}(d\chi_0^{-1}/d(T))^{-1}$ for LBCMO. β, γ and T_c are $\beta = 0.30954 \pm 0.0003$ with $T_c = 229.84$ K ± 0.1 and $\gamma = 1.016 \pm 0.001$ with $T_c = 230$ K ± 0.02 [Fig. 15(b)]. One can observe that the critical exponents acquired using the KF approach and the exponents derived using MAPs are in agreement. The critical exponents of LBCMO have also been determined using field dependent magnetic entropy change. For a SOPT, the field dependency of magnetic entropy change may be written as [43]

$$\Delta S_M = a(\mu_0 H)^n, \tag{19}$$

where n is a function of the sample's magnetic state. Inset of Fig. 16(a) illustrates the linear plot $ln(|\Delta S_M|)$ vs ln (H) at T_c, which determines the value of n. It has been determined that n has a value of 0.5457. Now, the following relations are used to identify critical exponents [43]:

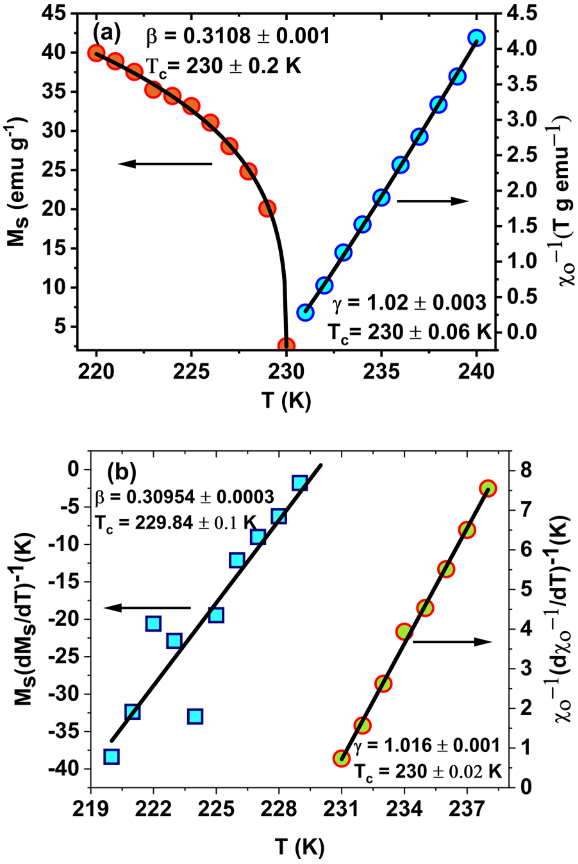

FIG. 15. (a) MAPs as a function of temperature for the inverse susceptibility $\chi_0^{-1}(T, 0)$ and the spontaneous magnetization $M_S(T, 0)$. (b) KF plots as a function of temperature for the $M_S(dM_S(T)/dT)^{-1}$ and $\chi_0^{-1}(d\chi_0^{-1}/d(T))^{-1}$.

$$n = 1 + \frac{1}{\delta}\left(1 - \frac{1}{\beta}\right), \tag{20}$$

$$n = 1 + \left(\frac{\beta - 1}{\beta + \gamma}\right), \tag{21}$$

Equations (11) are used to independently find the critical exponents δ. Figure 16(b) shows the isothermal M-H at T_c and inset shows log-log plot's linear fit in the higher field region. The log-log plot's slope of the linear fit specifies $1/\delta$, yielding $\delta = 4.20$. Further, the Eqs. (20) and (21) are used to get the critical exponents $\beta = 0.344$ and $\gamma = 1.11$, respectively. Additionally, the critical exponent for low temperature may be calculated by fitting Eq. (9) with M versus T(K) data, although it will be challenging due to ferromagnetic clustering. Then, using Eq. (12) to fit the $\frac{dM}{dT}$ plot, we may determine β. Figure 17 illustrates fitting, and the calculated value of β is 0.31.

When compared to the exponents calculated using the MAPs and KF technique, the values of the critical exponents (β and γ) match up nicely. Last but not least, Widom-scaling relation [57] employing Eq. (16) ensures the accuracy of the exponents. The exponents β, γ acquired from the MAPs and KF methods as well as the Widom-scaling relation were used

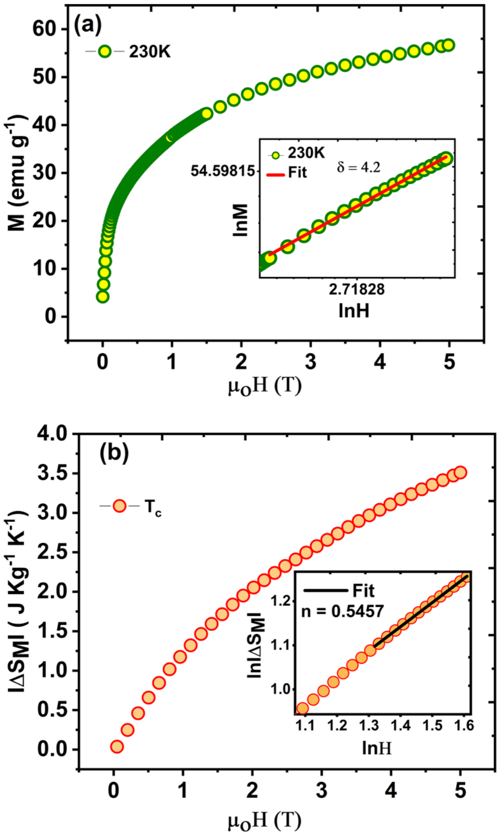

FIG. 16. (a) Equation $M = DH^{1/\delta}$ used for linear fitting of sample LBCMO's M-H isotherm at T_c (shown with red line) and log-log plot of M-H isotherm shown in inset. (b) Plot of LBCMO's $|\Delta S_M|$ as a function of field at T_c. log-log plot of LBCMO's $|\Delta S_M|$ with field and its linear fit (black line) have been shown in the inset.

to determine the δ value for LBCMO, which was found to be 4.281 and 4.282, respectively. As a result, the critical exponents determined using either technique are precise and unambiguous. Interaction phenomenon does not adhere to any universality class of interactions. If a physical system does not follow any universality class, it could suggest that the system has unique features that are not captured by the existing models. This could happen if the interactions between the system's constituents are too complex or if there are multiple competing interactions that cannot be described by a single model [58]. It may also result from the presence of defects caused by enhanced A-site disorder, formation of nanograins, or grain boundaries.

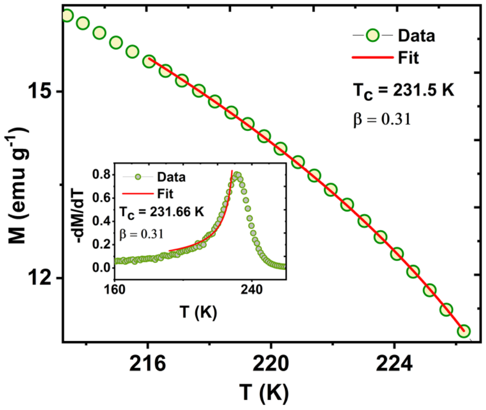

FIG. 17. LBCMO, magnetization vs temperature around 230 K. Inset shows the $\frac{dM}{dT}$ vs T(K) plot, fitted with Eq. (12) results $\beta = 0.31$.

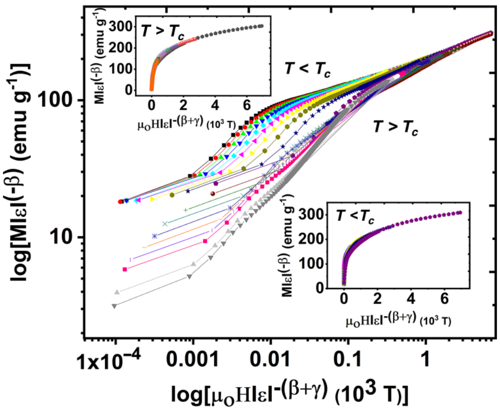

FIG. 18. Magnetization's scaling behavior is shown in the main panel as a function of renormalized H on a log-log scale ($T < T_c$ and $T > T_c$) for LBCMO. Renormalized H is shown in the upper and lower insets as a function of the renormalized fields $T > T_c$ and $T < T_c$, respectively.

These defects can cause short-range ferromagnetic interaction in a paramagnetic matrix, as observed in the case of GP [59]. Furthermore, the validity of the resulting exponents has also been confirmed by Eq. (14) using the notion of critical phenomena and the plot's data ($M\epsilon^{-\beta}$ vs $\mu_0 H\epsilon^{-(\beta+\gamma)}$) should flatten into two different curves below and above T_c [60]. Insets of Fig. 18 shows the scaling plot of renormalized magnetization m ($m = M\epsilon^{-\beta}$) and field, h ($h = \mu_0\, H\epsilon^{-(\beta+\gamma)}$) and two separate universal curves, one above and one below T_c, contain all the data. The field and scaled renormalized magnetization support the accuracy of the previous study.

Using Eq. (14) on a log-log scale, the main panel of Fig. 18 shows the scaling behavior of M and H values above and below T_c. The scaling equation of state suggests that the interactions are correctly renormalized in critical regimes. We also drew the MAPs from the MAPs approach for the values of $\beta = 0.3108$ and $\gamma = 1.02$. Figure 19 illustrates how all MAPs isotherms in higher field regions show as nearly parallel lines as they can. This is another confirmation of our LBCMO results.

IV. SUMMARY AND CONCLUSIONS

The structural, magnetic, and resistive characteristics of La$_{0.67-x}$Bi$_x$Ca$_{0.33}$MnO$_3$ ($x = 0.0$, 0.1) have been examined. Both materials exhibit a second-order PM-FM phase transition. The transition temperature decreases as Bi content increases in La site. The reduction of T_c is caused by the lone pair of Bi's 6s orbital. Studied samples exhibit short-range FM linked spin clustering, known as GP, above the transition temperature. The attenuation of GP caused by Bi doping is explained by a dimeron hypothesis. The existence of dimeron above T_{MI} was also confirmed by a temperature-dependent resistivity data and the sample show metal to insulator

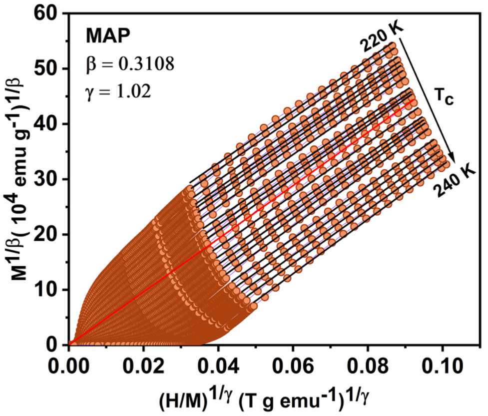

FIG. 19. MAPs $M^{\frac{1}{\beta}}$ vs $(\frac{H}{M})^{\frac{1}{\gamma}}$ at various temperatures near T_c for LBCMO.

transition. The order of the magnetic phase transition has been identified using the Arrott plots, Banerjee criterion, Landau theory, and magnetic entropy analysis. For LBCMO, critical scaling behavior has also been discussed and the values of the universal critical exponents (β, γ, and δ) have been calculated using the Arrott-Naokes and Kouvel-Fisher formula and it is validated using the Widom criterion. The employed methods provide exact and unambiguous critical exponents; the interactions seem to be correctly renormalized in critical regimes and do not adhere to any universality class of interactions.

ACKNOWLEDGMENTS

A.G. thanks CSIR for financial support through fellowship. We also want to thank AIRF, JNU along with CIF-SPS, JNU for measurements.

---

[1] M.-H. Phan and S.-C. Yu, J. Magn. Magn. Mater. **308**, 325 (2007).
[2] P. W. Anderson and H. Hasegawa, Phys. Rev. **100**, 675 (1955).
[3] A. J. Millis, P. B. Littlewood, and B. I. Shraiman, Phys. Rev. Lett. **74**, 5144 (1995).
[4] A. S. Alexandrov and A. M. Bratkovsky, J. Phys.: Condens. Matter **11**, 1989 (1999).
[5] A. P. Ramirez, J. Phys.: Condens. Matter **9**, 8171 (1997).
[6] C. Zener, Phys. Rev. **82**, 403 (1951).
[7] M. Respaud, J. M. Broto, H. Rakoto, J. Vanacken, P. Wagner, C. Martin, A. Maignan, and B. Raveau, Phys. Rev. B **63**, 144426 (2001).
[8] Y. Tokura, Rep. Prog. Phys. **69**, 797 (2006).
[9] R. Yamamoto, T. Furukawa, K. Miyagawa, T. Sasaki, K. Kanoda, and T. Itou, Phys. Rev. Lett. **124**, 046404 (2020).
[10] I. F. Mello, L. Squillante, G. O. Gomes, A. C. Seridonio, and M. de Souza, J. Appl. Phys. **128**, 225102 (2020).
[11] P. Moretti and M. A. Muñoz, Nat. Commun. **4**, 2521 (2013).
[12] Z. Xia, L. Xiao, C. Fang, G. Liu, B. Dong, D. Liu, L. Chen, L. Liu, S. Liu, D. Doyananda *et al.*, J. Magn. Magn. Mater. **297**, 1 (2006).
[13] S. Atalay, V. Kolat, H. Gencer, and H. Adiguzel, J. Magn. Magn. Mater. **305**, 452 (2006).
[14] A. Tozri, E. Dhahri, E. Hlil, and M. Valente, Solid State Commun. **151**, 315 (2011).
[15] J. Alonso, L. Fernández, F. Guinea, V. Laliena, and V. Martín-Mayor, Nucl. Phys. B **596**, 587 (2001).
[16] A. Tozri, E. Dhahri, and E. Hlil, Phys. Lett. A **375**, 1528 (2011).
[17] J. Khelifi, A. Tozri, E. Dhahri, and E. Hlil, J. Magn. Magn. Mater. **349**, 149 (2014).
[18] A. Gaur, Meenakshi, V. Nagpal, P. Bisht, and R. N. Mahato, Solid State Commun. **340**, 114504 (2021).
[19] R. Sanchez, J. Rivas, C. Vázquez-Vázquez, A. López-Quintela, M. Causa, M. Tovar, and S. Oseroff, Appl. Phys. Lett. **68**, 134 (1996).
[20] M. Pękała, V. Drozd, J.-F. Fagnard, P. Vanderbemden, and M. Ausloos, Appl. Phys. A **90**, 237 (2008).
[21] R. Seshadri and N. A. Hill, Chem. Mater. **13**, 2892 (2001).
[22] B. Banerjee, Phys. Lett. **12**, 16 (1964).
[23] C. Magen, P. A. Algarabel, L. Morellon, J. P. Araújo, C. Ritter, M. R. Ibarra, A. M. Pereira, and J. B. Sousa, Phys. Rev. Lett. **96**, 167201 (2006).
[24] A. J. Bray, Phys. Rev. Lett. **59**, 586 (1987).
[25] Y. Shimada, S. Miyasaka, R. Kumai, and Y. Tokura, Phys. Rev. B **73**, 134424 (2006).
[26] L. Downward, F. Bridges, S. Bushart, J. J. Neumeier, N. Dilley, and L. Zhou, Phys. Rev. Lett. **95**, 106401 (2005).
[27] F. Bridges, L. Downward, J. J. Neumeier, and T. A. Tyson, Phys. Rev. B **81**, 184401 (2010).
[28] H. C. Chauhan, B. Kumar, J. K. Tiwari, and S. Ghosh, Phys. Rev. B **100**, 165143 (2019).
[29] V. Franco, A. Conde, J. M. Romero-Enrique, and J. S. Blázquez, J. Phys.: Condens. Matter **20**, 285207 (2008).
[30] C. Romero-Muñiz, R. Tamura, S. Tanaka, and V. Franco, Phys. Rev. B **94**, 134401 (2016).
[31] V. Franco, A. Conde, V. K. Pecharsky, and K. A. Gschneidner Jr., Europhys. Lett. **79**, 47009 (2007).
[32] C. M. Bonilla, J. Herrero-Albillos, F. Bartolomé, L. M. García, M. Parra-Borderías, and V. Franco, Phys. Rev. B **81**, 224424 (2010).
[33] R. Guetari, T. Bartoli, C. Cizmas, N. Mliki, and L. Bessais, J. Alloys Compd. **684**, 291 (2016).
[34] R. Li, W. Tong, L. Pi, and Y. Zhang, J. Magn. Magn. Mater. **355**, 276 (2014).
[35] M. Wali, R. Skini, M. Khlifi, E. Dhahri, and E. K. Hlil, Dalton Trans. **44**, 12796 (2015).
[36] M.-H. Phan, S.-C. Yu, and N. H. Hur, Appl. Phys. Lett. **86**, 072504 (2005).
[37] H. E. Stanley, Rev. Mod. Phys. **71**, S358 (1999).
[38] L. Xu, J. Fan, Y. Zhu, Y. Shi, L. Zhang, L. Pi, Y. Zhang, and D. Shi, Mater. Res. Bull. **73**, 187 (2016).
[39] M. Pektas, T. Izgi, H. Gencer, S. Atalay, V. S. Kolat, and N. Bayri, J. Mater. Sci.: Mater. Electron. **31**, 15731 (2020).
[40] N. Dang, D. Kozlenko, G. Kim, W. Shon, J.-S. Rhyee, D. N. Petrov, T. Manh, and P. T. Long, Curr. Appl. Phys. **20**, 794 (2020).
[41] V. Franco, J. Blázquez, J. Ipus, J. Law, L. Moreno-Ramírez, and A. Conde, Prog. Mater. Sci. **93**, 112 (2018).

[42] D. Guo, L. M. Moreno-Ramírez, C. Romero-Muñiz, Y. Zhang, J.-Y. Law, V. Franco, J. Wang, and Z. Ren, Sci. China Mater. **64**, 2846 (2021).

[43] V. Franco, J. S. Blázquez, and A. Conde, Appl. Phys. Lett. **89**, 222512 (2006).

[44] V. Franco and A. Conde, Int. J. Refrig. **33**, 465 (2010).

[45] H. Oesterreicher and F. Parker, J. Appl. Phys. **55**, 4334 (1984).

[46] C. Romero-Muñiz, V. Franco, and A. Conde, Phys. Chem. Chem. Phys. **19**, 3582 (2017).

[47] M. Shimizu, Rep. Prog. Phys. **44**, 329 (1981).

[48] D. Kim, B. L. Zink, F. Hellman, and J. M. D. Coey, Phys. Rev. B **65**, 214424 (2002).

[49] S. Kaul, J. Magn. Magn. Mater. **53**, 5 (1985).

[50] K. Huang, *Introduction to Statistical Physics* (Chapman and Hall/CRC, Boca Raton, FL, 2009).

[51] H. E. Stanley, *Phase Transitions and Critical Phenomena* (Clarendon Press, Oxford, 1971), Vol. 7.

[52] A. Arrott and J. E. Noakes, Phys. Rev. Lett. **19**, 786 (1967).

[53] J. Fan, L. Ling, B. Hong, L. Zhang, L. Pi, and Y. Zhang, Phys. Rev. B **81**, 144426 (2010).

[54] L. Zhang, J. Fan, X. Zhu, W. Ning, Z. Qu, M. Ge, L. Pi, and Y. Zhang, Appl. Phys. A **113**, 201 (2013).

[55] M. E. Fisher, Rep. Prog. Phys. **30**, 615 (1967).

[56] J. S. Kouvel and M. E. Fisher, Phys. Rev. **136**, A1626 (1964).

[57] L. P. Kadanoff, Phys. Phys. Fiz. **2**, 263 (1966).

[58] H. C. Chauhan, B. Kumar, A. Tiwari, J. K. Tiwari, and S. Ghosh, Phys. Rev. Lett. **128**, 015703 (2022).

[59] S. Saha, A. Dutta, S. Gupta, S. Bandyopadhyay, and I. Das, Phys. Rev. B **105**, 214407 (2022).

[60] N. Khan, A. Midya, K. Mydeen, P. Mandal, A. Loidl, and D. Prabhakaran, Phys. Rev. B **82**, 064422 (2010).